Ice-shelf dynamics near the front of Filchner-Ronne Ice Shelf, Antarctica, revealed by SAR interferometry: model/interferogram comparison

Douglas R. MacAyeal, [1] Eric Rignot,[2] Christina L. Hulbe[3]

Received _____; accepted _____

Submitted to *Journal of Glaciology*, 1997.

Short title:

[2]Jet Propulsion Laboratory, California Institute of Technology, Pasadena, California 91109. (e-mail: eric@adelie.Jpl.Nasa.Gov)

[1]Department of Geophysical Sciences, University of Chicago, Chicago, Illinois 60637. (e-mail: drm7@midway.uchicago.edu)

[3]Department of Geophysical Sciences, University of Chicago, Chicago, Illinois 60637. (e-mail: chulbe@midway.uchicago.edu)

Abstract. We compare Earth Remote Sensing (ERS) satellite synthetic-aperture radar (SAR) interferograms with artificial interferograms constructed using output of a finite-element ice-shelf flow model to study the dynamics of Filchner-Ronne Ice Shelf (FRIS) near Hemmen Ice Rise (HIR) where the iceberg-calving front intersects Berkner Island (BI). We find that the model must account for rifts, mechanically competent sea ice which fills rifts, and ice softening in coastal boundary layers in order to agree with the ice deformation pattern implied by observed interferograms. Analysis of the stress field in the model experiment that best matches the observed interferograms suggests that: (1) HIR introduces weakness into the ice shelf through the generation of large-scale rifts, and (2) the melange of sea ice and ice-shelf fragments that fills the rifts stabilizes the shelf front by providing mechanical coupling between the fractured shelf front and the adjacent coast. The rift-filling melange could melt more easily than surrounding ice shelf and thus could represent a vulnerability of the FRIS to climate warming.

Introduction

As an initial effort to interpret SAR interferograms of the eastern flank of Ronne Ice Shelf's ice front (also referred to as the Filchner-Ronne Ice Shelf, or FRIS) described in a companion paper (Rignot and MacAyeal, this issue), we simulated the flow regime surrounding Hemmen Ice Rise (HIR) (Figure 1) using a finite-element model that accounts for gravitationally driven ice-shelf creep. The motivations for our modelling study were to: (1) construct artificial interferograms representing simplified flow regimes to compare with the real interferograms, (2) estimate physical parameters, such as the thickness of sea ice which fills rifts, by fitting model-generated interferograms to their real counterparts, and (3) to further validate the performance of the finite-element ice-shelf model in applications to the neighborhood of an iceberg-calving margin.

Using a trial-and-error technique, we found that artificial, model-generated interferograms can be fitted to observed interferograms if the model accounts for three features. First, the model must have the capacity to represent rifts of arbitrary geometry. This allows the stress regime in the wake of HIR to be relieved of shear stress. Second, the model must account for mechanically competent ice melange which fills larger, older rifts. Without including the melange, the model fails to reproduce the observed strain rates along the ice front or the rigid-body rotation of large ice-shelf fragments in the wake of HIR. Third, the model must allow for softer ice in coastal boundary layers surrounding HIR and neighboring Berkner Island (BI). This modification of ice-shelf viscosity may be related to strain heating, ice crystal alignment, crevassing, brine infiltration and tidal flexure.

Model Description

Ice-shelf flow is simulated in four experiments (Table 1) using the finite-element model named "Chicago 1" described by MacAyeal and others (1996). The model

used here was constructed and certified using EISMINT model-intercomparison standards as described by MacAyeal and others (1996). Thus, the agreement between model-generated and real interferograms demonstrated here provides an encouraging endorsement of the model formulation in common use.

The model provides a solution of the ice-shelf stress-equilibrium equations, but not the mass-balance or heat-transfer equations. Thus, the output of the model is the "snap shot" of velocity, strain-rate and stress fields determined by an input field consisting of the specified ice thickness distribution, h. Surface and basal temperatures and accumulation rates are not required as model input because the time-dependent thickness and temperature fields are not sought. Output variables of the model are u and v, the horizontal velocity components (x- and y-components, respectively, in a Cartesian coordinate system representing a Lambert equal-area map of the Antarctic). These components are assumed independent of the vertical coordinate (z).

Kinematic boundary conditions are specified along ice-shelf/grounded ice boundaries (*i.e.* around the edges of HIR and BI) and along artificial boundaries where the limited domain of the finite-element mesh terminates within the interior of the FRIS. Along the edges of HIR and BI, where floating ice shears past grounded inland ice, a zero-flow condition is applied as suggested by the SAR interferograms, which display near-zero displacement within the central portions of HIR and BI.

At the seaward ice front, including the interior boundaries defining rifts when modelled as being free of sea ice, the pressure of sea water is specified as a boundary condition:

$$\int_b^s \mathbf{T} \cdot \mathbf{n} dz = \frac{\rho_w g}{2} (\frac{\rho}{\rho_w} h)^2 \mathbf{n} \tag{1}$$

where s and b are the ice-shelf surface and basal elevations, respectively, and assumed to be in hydrostatic equilibrium (*i.e.,* $b = \frac{-\rho h}{\rho_w}$), $\mathbf{T}$ is the stress tensor, $\mathbf{n}$ is the outward-pointing normal to the ice-front contour in the horizontal plane, $g = 9.81$ m

s^{-2} is the gravitational acceleration, and $\rho_w = 1028$ kg m^{-3} is the density of seawater (assumed uniform).

Ice is assumed to be incompressible and to deform according to an effective viscosity ν representing Glen's flow law. Following Hooke and others (1979; see also MacAyeal and Thomas, 1986)

$$\mathbf{T}' = 2\nu\dot{\mathbf{e}} \tag{2}$$

where $\mathbf{T}'$ is the deviatoric stress and $\dot{\mathbf{e}}$ is the strain rate. The definition of ν involves a temperature-dependent rate variable $\bar{B}$, a flow-law exponent n, and an evaluation of the second invariant of the strain-rate tensor that disregards second-order components (*i.e.,* vertical shear):

$$\nu = \frac{\bar{B}}{2\left[\left(\frac{\partial u}{\partial x}\right)^2 + \left(\frac{\partial v}{\partial y}\right)^2 + \frac{1}{4}\left(\frac{\partial u}{\partial y} + \frac{\partial v}{\partial x}\right)^2 + \frac{\partial u}{\partial x}\frac{\partial v}{\partial y}\right]^{\frac{n-1}{2n}}} \tag{3}$$

The flow-law rate variable $\bar{B}$ represents a depth-averaged parameter which can vary considerably over the ice shelf as a result of temperature and density variation (*e.g.,* Thomas and MacAyeal, 1982; MacAyeal and Thomas, 1986). The flow-law exponent n is assumed to be 3.

The flow-law rate variable $\bar{B}$ is assumed to be uniform in Experiments 1 - 3 and is varied in narrow boundary layers in Experiment 4. Specifying a uniform $\bar{B}$ avoids the necessity of estimating ice temperature, crystal fabric, density and other influences on ice flow that would lead to spatial variation of ice hardness. A good fit between model and observed velocity in the broad-scale simulation of the entire FRIS is obtained with $\bar{B} = 2.1 \times 10^8$ Pa $s^{-\frac{1}{3}}$. This value corresponds to that expected for isotropic polycrystalline ice at a temperature of approximately 253 K, and is comparable to the value used to simulate flow of the Ross Ice Shelf ($\bar{B} = 1.9 \times 10^8$ Pa $s^{\frac{-1}{3}}$, as reported by MacAyeal and others, 1996). Spatial refinement of the rate constant factor to improve the fit between model-derived flow and the observed interferograms would require a control method, or some other data-fitting technique (*e.g.,* Rommelaere and MacAyeal,

1997). In Experiment 4 (soft ice), $\bar{B}$ is reduced to 1.05×10^8 Pa $s^{-\frac{1}{3}}$ within coastal boundary layers surrounding HIR and BI to simulate the effects of ice softening in a region of intense shear and perhaps brine infiltration.

Model Input Data

Ice thickness h is specified using the the British Antarctic Survey (BAS) gridded analysis (Vaughan and others, 1995, 1994). The grid resolution of the BAS analysis is approximately 2.8 km. The effects of a firn layer are not treated explicitly by the model, so total ice thickness provided by the BAS data was reduced by 14 m, the assumed thickness of the air column contained within the firn layer. Ice thickness in the BAS gridded analysis was derived from ERS-1 ice surface altimetry (Vaughan and others, 1995). Over the interior of the ice shelf, the uncertainty of h is approximately 70 m. The BAS gridded analysis does not cover the region between HIR and BI, where the altimetry was degraded by strong surface slopes. To specify h in this region, we extrapolated using a linear variation that represents the average trend of ice thickness through the study area (*i.e.,* following the ice thickness trend along the flowline passing just west of HIR where the BAS gridded analysis was adequate). We are unable to estimate the uncertainty associated with the ice-thickness extrapolation, because the region of disturbed ice between HIR and BI is least likely to follow the general thickness trends of the ice shelf. We suspect, however, that it is probably much greater than the 70 m uncertainty applicable for the rest of the ice shelf. This high level of uncertainty is unlikely to have a major effect on the conclusions of our study, because they are qualitatative for the most part.

Finite-Element Discretization

The study region is represented by meshes of 3-node triangular elements as shown

in Figures (2) - (4). Three different finite-element meshes are used in Experiments 1 - 3. Experiment 4 employs the same network as Experiment 3, because boundary-layer ice softening could be treated without changing the mesh geometry. Horizontal resolution within each model mesh varies from approximately 300 m near HIR to about 15 km near upstream boundaries where kinematic boundary conditions are applied. The primary differences between the three finite-element meshes are the geometry of rifts and the coverage of sea-ice filled areas between ice-shelf fragments. Within each element, horizontal velocities vary linearly with x and y; and the vertical velocity, w, and strain rate tensor, $\dot{\mathbf{e}}$, are constant. Thickness h is specified at mesh nodes (triangle vertices).

Boundary conditions needed by the model are specified on all exterior boundaries of the various meshes used for Experiments 1 - 4. For Experiment 2, in which rifts were assumed open and filled with nothing other than seawater, the dynamic boundary condition representing the hydrostatic pressure force exerted by water on the subsealevel faces of the rifts and expressed by Equation (1) was used. In Experiments 3 and 4, boundary conditions were not needed at the edges of rifts filled with ice melange, because the ice melange/ice shelf transition did not form an exterior boundary of the finite-element domain. The ice melange/ice shelf transition was treated by specifying a step-like change in ice thickness (from a variable value greater than 100 m on the ice-shelf side of the transition, to 10 m on the ice-melange side of the transition).

Mesh Nesting Scheme

Restricting the model domain to the region around HIR (see Figure 5) allows us to concentrate computational efforts and increase mesh resolution in the study area. The kinematic and dynamic influence of the entire FRIS on the model area is retained through open boundaries and specified kinematic boundary conditions within the interior of the FRIS (Figure 5). The boundary condition (velocity) is derived from the flow field produced by a low-resolution finite-element model of the entire FRIS

(Figure 5). Each limited-domain open boundary node lies within an element of the larger "far-field" mesh. Velocity components u and v at each open boundary node are linearly interpolated from values of u and v at the nodes of the surrounding far-field mesh element. The far-field FRIS simulation is performed using the same numerical model as is used to simulate flow within the limited HIR domain and with the same physical parameters (ρ, ρ_w and uniform $\bar{B}$). Boundary conditions for the low-resolution FRIS simulation are of the dynamic type for seaward margins (Equation 1), or of the kinematic type for inland margins. Velocity specified along inland margins was zero except for three ice-stream inlets (Rutford, Evans and Foundation ice streams). Ice-stream inlet velocities were taken from the study by Vaughan and others (1995).

Accuracy of the open boundary condition may be evaluated by comparing simulated large-scale flow with the observed flow of the ice shelf (Vaughan and others, 1995). The simulated and observed flow in the region surrounding the HIR agreed within approximately 50 m a^{-1}, or about 5%. This is sufficient for the specification of boundary conditions on the nested model. Further improvement would require considerable effort to estimate a spatially variable $\bar{B}$ accounting for the rheological effects of ice temperature variations and marine ice (*e.g.,* Lange and MacAyeal, 1986).

Model Performance Criteria

The ice-shelf modelling experiments were originally structured to identify which aspects of ice dynamics, ice rheology, boundary conditions, and oceanic forcing would be most relevant in the interpretation of the SAR interferometric observations. At the outset, we were skeptical that such a prioritization could be produced, because there are substantial uncertainties associated with model input parameters (*e.g.,* present-day thickness, ice temperature, and boundary conditions) that are well-known controls on ice-shelf flow. An additional concern was that motions detected by SAR

interferometry arise from a mixture of physical processes while the long-term ice-shelf flow (gravitationally driven creep) simulated by the model is only one contributor to that motion. Tidal flexure and other short-term motions introduced by ocean swell and currents contaminate the signal of ice-shelf creep flow in the interferograms, and could possibly mislead our effort to match model to observation. Our greatest concern was that the interferograms would not provide suitable model-fitting targets because our model simulates only a limited number of the many physical processes involved in ice-shelf motion.

Experience and good luck (*i.e.,* optimal SAR data, as described by Rignot and MacAyeal, this issue) allowed us to fit the model flow regime to that implied by the SAR interferograms, and allowed us to prioritize the ice-shelf processes most important in governing flow near HIR and the ice front. Three processes, listed below, emerged as essential ingredients in model experiments that agreed most favorably with the SAR interferograms.

1. Ice-shelf fragmentation, such as caused by rifts;

2. Permanent sea ice which fills rifts and binds partially detached ice-shelf fragments (as described in the companion paper by Rignot and MacAyeal, this issue);

3. Ice softening in shear margins surrounding the ice rise and coastal boundaries, caused by strain heating or some other process.

Our treatment of model input information, such as ice thickness and large-scale flow-parameter variation related to density, temperature and ice salinity, also influenced the favorable fit between model and SAR observation. However, these well-known influences were anticipated as a result of low-resolution observations made in the past with other methods (*e.g.,* Lange and MacAyeal, 1986). We thus focus our summary of model experimentation on an illustration of how the above three processes in particular

influence the fit between model and SAR interferograms.

Artificial, Model-Derived Interferograms

Model performance is measured by comparison between artificial interferograms constructed using model output and the observed target interferograms (presented by Rignot and MacAyeal, this issue). Although some quantitative measures of these comparisons are presented below, our main objective was to produce model runs which produced artificial interferograms that had a good visual resemblance to the observed interferograms.

Artificial interferograms were constructed by transferring the horizontal velocity components, u and v, from the finite-element mesh to the rectangular arrays of pixels representing the SAR interferograms associated with ascending and descending orbital geometries. Model velocity for each pixel was used to compute the horizontal displacement of the ice-shelf surface over a 1-day temporal baseline. The 1-day time span reduces the total number of fringes displayed in the interferogram to a visually comprehensible number (*e.g.,* from order 90 to order 30). Use of a 1-day baseline for comparison purposes required adjustment of the actual SAR interferograms presented in Rignot and MacAyeal (this issue), which involved actual temporal baselines ranging from 1 to 9 days.

The 1-day surface displacement predicted by the model was converted to an interferogram using the orbit geometry (as described by Rignot and MacAyeal, this issue) and pixel location relative to the geographic coordinate system used to process the observed SAR imagery. The interferometric phase difference, ϕ, is determined from model velocity using the following expression,

$$\phi = \frac{4\pi}{\lambda}\sqrt{u^2 + v^2}\Delta t \cos\psi \sin\theta \ , \tag{4}$$

where $\lambda = 5.66$ cm is the ERS satellite SAR wavelength, Δt is the time span of

displacement (1 day), θ is the local angle of incidence of the radar (about 23 ° from zenith) given by

$$\theta = \arccos\left(\frac{-r^2 + Z_s^2 - (R+s)^2}{2r(R+s)}\right) , \quad (5)$$

where r is the range distance to the satellite, Z_s is the distance between the satellite and the center of the earth, R is the earth curvature at nadir, s is the surface elevation (taken to be zero), and ψ is the angle between the horizontal ice velocity and the projection of the SAR range direction into the horizontal plane (see Equation 2 of Rignot and MacAyeal, this issue).

Model Experiments

Agreement between artificial, model-generated interferograms and observed, target interferograms was found by trial and error. Model assumptions, parameters and finite-element mesh geometries were varied until a "satisfactory fit" was obtained between model and data. More advanced techniques, such as the control method used by Rommelaere and MacAyeal (1997) to estimate rheological parameters of the Ross Ice Shelf, were inappropriate for this study, because there were too many uncertainties associated with model-input parameters and tidal contamination of the interferograms. The subjective trial-and-error approach used here allowed us to achieve our goal of prioritizing ice-flow processes and conducting sensitivity tests for demonstration.

Numerous trial-and-error experiments were necessary to determine structural features and dynamic processes most influential in determining the quality of fit between observed and synthetic interferograms. For clarity, 4 representative experiments are discussed here. The 4 experiments are a control and 3 variations, which demonstrate the sensitivity of model performance to rifting, rift filling by mechanically competent ice melange and ice softening in coastal boundary layers. Unique features of the 4 experiments are summarized in Table (1).

The artificial interferograms generated from Experiments 1 to 4 are presented in Figures (6) and (7). Difference between the artificial interferograms generated using results of Experiment 4 (the closest match) and the observed interferograms is presented in Figure (8). A quantitative assessment of model performance was made by computing a scalar variable X^2 defined by

$$X^2 = \frac{1}{A_{\text{image}}} \int\int_{\text{full image}} \frac{(\phi_m - \phi_o)^2}{\sigma^2} dxdy \ , \tag{6}$$

where ϕ_o and ϕ_m are the unwrapped phase fields of the observed and the model-generated interferograms, respectively, and $\sigma = \frac{\pi}{14}$ is the estimated standard deviation of ϕ_o due to random observation error and unwrapping-algorithm error. The domain of integration of X^2 is approximately 80 % of the area of the observed interferograms (regions where the observed phase could not be unwrapped reliably were excluded from the integration). Another scalar variable, X^2_{HIR}, is defined in a manner similar to X^2, however, the area of integration in Equation (6) is reduced to the 40×40 km rectangle of pixels containing HIR and the zones of the ice shelf where ice softening is modelled in Experiment 4.

The numerical values of X^2 and X^2_{HIR} are presented in Table (2). The greatest change in model performance using the X^2 measure is between Experiments 2 and 3 in the descending-pass interferogram comparison. The 12-fold decrease in X^2 from Experiment 2 to Experiment 3 is mostly due to the improvement of the model-derived interferograms in the region downstream of HIR where the inclusion of rift-filling ice melange had its greatest effect. This 12-fold improvement constitutes the strongest support for the qualitative conclusion we reach below that ice melange has an important influence on ice-shelf flow near the ice front of the FRIS. Improvements in the X^2 measure of model/data misfit for the ascending-pass geometry were primarily between Experiments 1 and 2. The reduced sensitivity of model performance to the presence of ice melange in the case of ascending-pass interferograms is due to the fact that the ascending-pass SAR images did not cover much of the region downstream of HIR where

the influence of ice melange is greatest.

Another notable improvement in model performance is seen in the X^2_{HIR} measure between Experiments 3 and 4 in the descending-pass interferogram comparison. This improvement is not as large as the improvement associated with the difference between Experiments 1 and 2. Nonetheless, it suggests that the influence of ice softening in narrow boundary layers along HIR is significant.

Effects of Ice-Shelf Rifts

The control experiment (Experiment 1) treated HIR as an island surrounded by a contiguous, rift-free ice shelf. A no-slip condition was applied around the coasts of HIR and BI. A uniform ice thickness, $h = 200$ m, was used instead of the BAS data to eliminate the indirect influence of rifts on flow due to thickness variations they may cause in the gridded analysis. The fringe lines of the synthetic interferogram constructed for Experiment 1 are continuous throughout the model domain (Figures 6 and 7).

Rifts visible in the SAR amplitude imagery (and apparent from fringe discontinuities in the interferograms) were explicitly represented in the finite-element mesh geometry of Experiment 2 (Figure 3). They were assumed to be filled with seawater, and the dynamic boundary condition (seawater pressure) was applied around the edges of these features. Singularities in the stress and strain-rate fields at rifts tips that cannot be resolved by the finite-element mesh, if any, were disregarded. Ice-shelf fragments which are surrounded by water were assigned a zero-velocity reference at a single node at their centers. A no-slip condition was applied around HIR and along the coast of BI, as in Experiment 1. Ice thickness is specified from the BAS gridded analysis.

An improvement in model performance can be seen by comparing the artificial interferograms generated for Experiment 2 with those of Experiment 1 (Figures 6 and 7). The discontinuities in fringe lines and changes in fringe-line spacing across rifts

produced in Experiment 2 are similar to those present in the observed interferograms (see Figure 8, of Rignot and MacAyeal, this issue).

A notable defect in Experiment 2 is insufficient rigid-body rotation (indicated by compressed parallel fringe lines oriented in the SAR-range direction, see Equation 5 and Figures 10 and 11 of Rignot and MacAyeal, this issue) in the ice-shelf fragments arrayed along BI downstream of HIR. Rigid-body rotation can be transmitted to the ice-shelf fragments by two mechanisms: (1) vorticity transmission across narrow "ice bridges" which connect the fragments to the ice shelf, and (2), drag induced by mechanically competent rift-filling sea ice which binds the fragments to the faster moving ice shelf to the west.

The first mechanism may be explained by examining the dynamics of vorticity in the flow of viscous fluids. Assuming that ν and h are constant within ice-shelf fragments,

$$\nabla^2 \zeta = 0, \tag{7}$$

where

$$\zeta = \frac{\partial u}{\partial y} - \frac{\partial v}{\partial x} \tag{8}$$

is the vorticity of the ice-shelf flow. Uniform ζ is associated with a rigid-body rotation, *i.e.,*

$$\zeta = 2\Omega, \tag{9}$$

where $\Omega = \frac{2\pi}{T_r}$ is the angular velocity of the rotation, and T_r is the period of rotation. A solution of Equation (7) is $\zeta(x, y) = \zeta_o$, where ζ_o is a constant. The value of ζ_o for ice-shelf fragments downstream of HIR is determined by the vorticity of the flow at the ice bridge denoted by the arrow in Figure(1). A no-slip condition is specified along the margin of BI (in Experiment 2), so the vorticity at the ice bridge is determined by the shear strain rate in the coastal boundary layer of the ice shelf along BI, *i.e.,*

$$\zeta_o = \dot{e}_{xy}, \tag{10}$$

where $\dot{e}_{xy}$ is the shear component of the strain-rate tensor. This is the only vorticity source for ice-shelf fragments in Experiment 2; so, as anticipated by the above analysis, fringe spacing within all ice-shelf fragments connected to the ice bridge is uniform and equal to that which appears at the ice bridge.

The model-derived rigid-body rotation rate of ice-shelf fragments in Experiment 2 is smaller than the observed rotation rate (see Figures 6 and 7). This inadequacy may be attributed to two causes. First, ζ_o at the ice bridge may be too low. This can be corrected by modifying boundary conditions so that the model flow has more shear along BI. Second, additional vorticity may be transmitted to the fragments by boundary traction along their edges elsewhere. This traction is likely supplied by the ice melange which binds the fragments to the faster flowing ice shelf passing west of HIR.

Effects of Rift-Filling Ice Melange

In Experiment 3, rifts and void space surrounding ice-shelf fragments were filled with a permanent, multiyear sea ice, which we call "ice melange". An observed value was unavailable, so we assumed the sea-ice thickness to be 10 m. The melange was modelled using the same governing equations and rheologic parameters ($\bar{B} = 2.1 \times 10^8$ Pa $s^{-\frac{1}{3}}$, $n = 3$) as used to model the ice shelf. The only aspect of the melange that made it different from the surrounding ice shelf was its reduced thickness.

The finite-element mesh for Experiment 3, Figure (4), incorporates both melange-filled and open rifts. Open rifts were necessary to capture fringe-line discontinuities discussed above. Two improvements of Experiment 3 over Experiment 2 are displayed in Figures (6) and (7). First, melange improves the rigid-body rotation of the ice-shelf fragments along the edge of BI. Second, melange improves the fringe-line density near the ice front west of HIR. Both improvements suggest that the rift-filling melange has mechanical integrity and serves to couple the fast flowing ice west of HIR to the coast

of BI.

The idealized rheological treatment of ice melange in Experiments 3 and 4, *i.e.,* that it is simply thin ice shelf with the same flow law and flow parameters, was motivated by the fact that no modifications to our model would be necessary to perform the experiments. Sensitivity studies (not presented here) suggested that qualitatively similar results could be obtained for ice-melange thicknesses in the range of 5 to 50 m. We did not explore the sensitivity of model results to other rheological treatments of the ice melange such as involving brittle deformation (*i.e.,* like sea ice).

Effects of Ice Softening

The effect of ice softening along the ice shelf margin was examined in Experiment 4. Almost all model parameters used in Experiment 4 were the same as those used in Experiment 3, including the geometry of the finite-element mesh. The feature that distinguishes Experiment 4 from Experiment 3 is the reduction of $\bar{B}$ along the sides of HIR and the coast of BI as shown in Figure (4). The value of $\bar{B}$ in elements along the boundaries was reduced to 1.05×10^8 Pa $\mathrm{s}^{\frac{-1}{3}}$, or to 50 % of the value in the surrounding ice shelf and ice melange.

The reduction of $\bar{B}$ was motivated by two factors. First, the comparison between artificial and observed interferograms in Experiment 3 indicated that the simulated ice-shelf flow between HIR and BI was too slow and that the shear layer on the western side of HIR appears to be too wide. Ice softening tends to correct these defects. The second motivating factor was that ice softening is often associated with boundary shear elsewhere in ice-shelf and ice-stream environments.

Softening in the shear margins of ice stream B, West Antarctica, was reported by Echelmeyer and others (1994). They found that a "flow enhancement" (their terminology for "ice softening") ranging up to a factor of 12 was required to explain

strain-rate measurements. This large enhancement was attributed to the combined effects of strain heating and development of aligned ice crystal fabric. Echelmeyer and others (1994) suggested that as much as 45 % of the total flow enhancement could be attributed to strain heating, depending on assumptions.

We assessed the potential for ice softening along HIR and BI due to strain heating. The depth-average strain-heating rate, $\bar{Q}$, is

$$\bar{Q} = \frac{1}{h} \int_b^s \dot{\mathbf{e}} \cdot \mathbf{T}' dz \tag{11}$$

where $\cdot$ denotes the tensor double dot product. Strain-heating rates computed for Experiment 4 (Figure 9) suggest that the margin of the HIR could be sufficiently heated to soften the ice.

The strain-heating rates near HIR in Experiment 4 are comparable in magnitude to the 10^{-3} W m^{-3} cited by Echelmeyer and others (1994). The warming rate estimated by Echelmeyer and others (1994) for their field application is 1.4 K per 100 years of ice residence time. The residence time for ice within the zone of strain heating near HIR is approximately 200 years. Multiplication of the warming rate by the residence time gives a net temperature rise that translates to an ice softening (*i.e.,* reduction of $\bar{B}$) of about 10%. It is possible that longer residence times along the coast of BI would allow a more substantial strain-heating effect.

Factors in addition to strain heating must also be occurring to account for the degree of softening implied by the artificial/observed interferogram comparison. These may include preferred fabric orientation (due to stresses associated with flow and tidal flexure), crevassing by tidal flexure, strain heating by tidal flexure, solar heating of the walls of surface crevasses, and the infiltration of salt water (which introduces heat as well as salt) through basal crevasses. Our results do not suggest which of these processes are likely contributors to the boundary-layer softening. However, they do provide an estimate of the overall degree of softening necessary to achieve adequate

model performance.

Summary and Discussion

The most significant result of this study is its support of the principal conclusion of the companion paper (Rignot and MacAyeal, this issue), namely, that ice melange, the mixture of sea ice, ice-shelf fragments and windblown snow that fills rifts and chasms, has a significant influence on the dynamics of the FRIS near the calving front. Model experiments presented here show that filling rifts with ice melange, even melange with idealized rheological properties, produces the largest improvement in model fidelity to observation. Ice melange in the wake of HIR clearly provides a strong mechanical coupling between the integrated, unfractured part of the ice shelf west of HIR and the ice-shelf fragments along the coast of BI. Secondary results of this study are that ice softening in coastal boundary layers around HIR and BI may be a significant and that this softening may be related to strain heating, among other processes.

Recognition of the importance of rift-filling ice melange prompts the question of how its presence influences the ice-rise buttressing forces generated by HIR. As suggested by Thomas (1979), ice rises may be essential to the stability of ice shelves. In comparison with Crary Ice Rise (CIR) on the Ross Ice Shelf, the buttressing influence of HIR is small (MacAyeal and others, 1987, 1989). Using the definition of dynamic drag, $\vec{F}_d$, introduced by MacAyeal and others (1987), the present model experiments show that the magnitude of $\vec{F}_d$ generated by HIR (in Experiment 1) is less than about 15% of that generated by CIR. The fact that HIR generates less dynamic drag is associated with the fact that HIR is smaller than CIR. (Form drag, defined by MacAyeal and others, 1987, is not discussed here because of the large uncertainty of ice thickness surrounding HIR.)

The most interesting aspect of the dynamic drag analysis is comparison of its magnitude, $|\vec{F}_d|$, among the 4 experiments presented here. This comparison is shown

in Table (3). Dynamic drag magnitude is greatest in Experiment 1 where rifts are not present. The reduction of dynamic drag in response to rifting is striking. With the introduction of open, melange-free rifts, $|\vec{F}_d|$ is reduced in Experiment 2 to approximately 15% of that in Experiment 1. This comparison suggests that the rifting process could be an important control on the buttressing forces induced by ice rises.

Comparison of Experiments 2 and 3 in Table (3) demonstrates that ice melange within rifts has an insignificant direct influence on the dynamic drag generated by HIR. The value of $|\vec{F}_d|$ is increased when melange is present, as is expected for the idealized treatment of melange in this study (*i.e.,* as thin ice shelf), but this increase is only about 1% . As speculated by Rignot and MacAyeal (this issue), the most important influence of ice melange on ice-shelf stability may be indirect; *i.e.,* through the supression of the rifting process. As suggested by the comparison of $|\vec{F}_d|$ for Experiments 1 and 2 (Table 3), even a small reduction in the amount of rifting around an ice rise may lead to a large pay off in terms of the maintenance of the ice-rise buttressing effect. If ice melange is part of a natural annealing process in which the tendency for an ice shelf to fracture and rift is reduced, then the potential vulnerability of melange to atmospheric and oceanic warming may be one way in which climate change can influence indirectly ice-shelf stability.

Acknowledgments

Work performed at the Jet Propulsion Laboratory, California Institute of Technology was supported by a contract from the National Aeronautics and Space Administration (NASA). Support for research conducted at the University of Chicago was provided by the European Space Agency (ERS-1/2 project code: AO2.USA.160), the National Aeronautics and Space Administration (NASA) of the U.S. (grant NAGW-5005, and a NASA Graduate Student Fellowship awarded to C. L. Hulbe). We thank Andrew

Gabriel for help in the project inception and comments through the research period. David Vaughan, Chris Doake, Richard Frolich, Richard Hindmarsh and other colleagues at the British Antarctic Survey provided ice-thickness data for the FRIS and many suggestions during the course of the research. We thank Charlie Werner, at JPL, for providing us with a SAR processor to process the ERS data used here and in the companion paper. We thank two anonymous referees for help in revising this and the companion paper.

References

Echelmeyer, K. A., W. D. Harrison, C. Larsen and J. E. Mitchell, 1994. The role of the margins in the dynamics of an active ice stream. *J. Glaciol.*, **40**, No. 136, 527-538.

Hooke, R.L., C. F. Raymond, R. L. Hotchkiss, and R. J. Gustafson, Calculations of velocity and temperature in a polar glacier using the finite-element method. *J. Glaciol.*, **24**, No. 90, 131-46.

Hulbe, C. L., E. Rignot and D. R. MacAyeal, in press. Comparison of ice-shelf creep flow simulations with ice-front motion of Filchner-Ronne Ice Shelf, Antarctica, detected by SAR interferometry. *Annals of Glaciology*, Hobart issue.

Jaeger, J. C., 1969. *Elasticity, fracture and flow. Third edition.* London, Methuen.

Lange, M. A. and D. R. MacAyeal, 1986. Numerical models of the Filchner-Ronne Ice Shelf: An assessment of re-interpreted ice thickness distributions, *Journal of Geophysical Research*, **91**(B10), 10457-10462.

MacAyeal, D. R. and R. H. Thomas, 1986. The effects of basal melting on the present flow of the Ross Ice Shelf, *Journal of Glaciology*, **32**(110), 72-86.

MacAyeal, D. R., R. A. Bindschadler, S. Shabtaie, S. Stephenson and C. R. Bentley, 1987. Force, mass and energy budgets of the Crary Ice Rise complex, Antarctica. *J. Glaciol.*, **33**, No. 114, 218-230.

MacAyeal, D. R., R. A. Bindschadler, S. Shabtaie, S. Stephenson and C. R. Bentley, 1987. Correction to: force, mass and energy budgets of the Crary Ice Rise complex, Antarctica. *J. Glaciol.*, **35**, No. 119, 151-152.

MacAyeal, D. R. and 5 others, 1996. An Ice-Shelf Model Test Based on the Ross Ice Shelf. *Annals of Glaciology*, **23**, 46-51.

Rignot, E. and D. R. MacAyeal, submitted. Ice-shelf dynamics near the front of Filchner-Ronne Ice Shelf, Antarctica, revealed by SAR interferometry. *J. Glaciol.*, submitted.

Rommelaere, V. and D. R. MacAyeal, 1997. Large-scale rheology of the Ross Ice Shelf, Antarctica, computed by a control method. *Annals of Glaciology*, **24**, in press.

Thomas, R. H., 1979. Ice shelves: a review. *J. Glaciol.*, **24**, No. 90, 273-286.

Thomas, R. H. and D. R. MacAyeal, 1982. Derived characteristics of the Ross Ice Shelf, Antarctica. *Journal of Glaciology*, **28**(100), 397-412.

Vaughan, D. G., J. Sievers, C. S. M. Doake, H. Hinze, D. R. Mantripp, V. S. Pozdeev, H. Sandhager, H. W. Schenke, A. Solheim and F. Thyssen, Subglacial and seabed topography, ice thickness and water column thickness in the vicinity of Filchner-Ronne-Schelfeis, Antarctica. *Polarforschung* **64** (2): 75-88 (1995).

Vaughan, D. G., J. Sievers, and 10 others, 1994. Map of Subglacial and Seabed Topography 1:2 000 000 Filchner-Ronne-Schelfeis / Weddell Sea, Antarctis. Institut fur Angewändte Geodäsie, Frankfurt am Main.

This manuscript was prepared with the AGU LaTeX macros v3.1.

Figure 1. Map of the study area. Radar range directions for the two orbital geometries (a: ascending, d: descending) are indicated with arrows. Gray areas represent grounded, stagnant ice. Black areas represent seasonal or permanent sea ice.

Figure 2. Finite-element mesh of Experiment 1 in the vicinity of HIR. For this experiment, there are 7,563 nodes and 14,437 elements in the complete limited domain.

Figure 3. Finite-element mesh of Experiment 2 in the vicinity of HIR (the complete limited domain has 12,469 elements and 6,902 nodes).

Figure 4. Open rifts and open water (black shading), rift-filling melange (gray shaded elements) and soft-ice boundary layers (gray shading) in Experiments 3 and 4.

Figure 5. Upper panel: finite-element mesh covering the entire FRIS (11,033 elements and 6,050 nodes). Lower panel: simulated velocity magnitude of the FRIS (contour interval =100 m a^{-1}). Kinematic boundary conditions required along open boundaries of the limited domain of Experiments 1 - 4 (heavy black line) were taken from this velocity field. Black areas denote open or sea-ice covered water, gray areas denote grounded ice.

Figure 6. Observed ERS and artificial interferograms for descending-pass orbital geometry. The arrow labeled "R" denotes SAR range direction.

Figure 7. Observed ERS and artificial interferograms for ascending-pass orbital geometry. The arrow labeled "R" denotes SAR range direction.

Figure 8. Difference between artificial and observed interferograms for Experiment 4 for ascending and descending orbital geometries (upper and lower panels, respectively).

Figure 9. Depth-average strain-heating rate computed for Experiment 4 (contour interval = 5×10^{-4} W m^{-3}).

Model Experiment	Short Name	Feature
1	Control	contiguous ice-shelf cover surrounding HIR and its wake, $h = 200$ m
2	Rifts	rifts modelled with seawater fill
3	Ice Melange	rifts filled with ice melange 10 m thick
4	Soft Ice	20 % ice softening in boundary layers of HIR and BI

Table 1. Numerical Experiments.

Model Experiment	ascending		descending	
	X^2	X^2_{HIR}	X^2	X^2_{HIR}
1	12230	17316	42498	42507
2	2026	5977	40959	1785
3	1843	6002	3404	1544
4	1823	5858	3439	850

Table 2. Model performance measures (comparison made to 6-day interferogram reported by Rignot and MacAyeal, this issue).

Model Experiment	$\lvert\vec{F}_d\rvert$ 10^{11} N
1	16.30
2	2.54
3	2.56
4	2.46

Table 3. Model-derived buttressing forces for HIR.

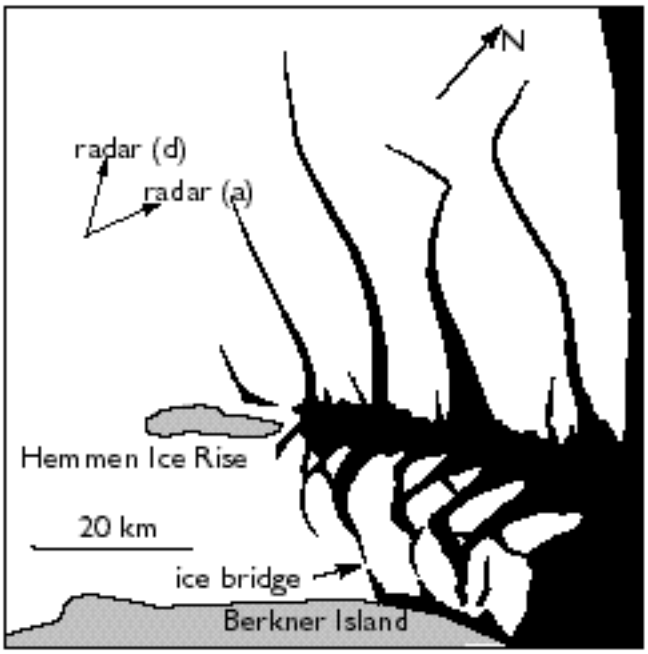
N
radar (d)
radar (a)
Hemmen Ice Rise
20 km
ice bridge
Berkner Island

Figure 1.

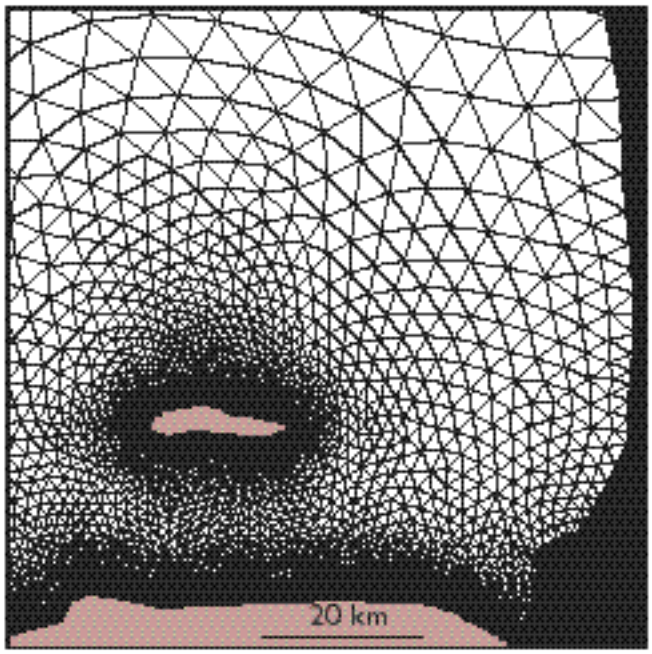

Figure 2.

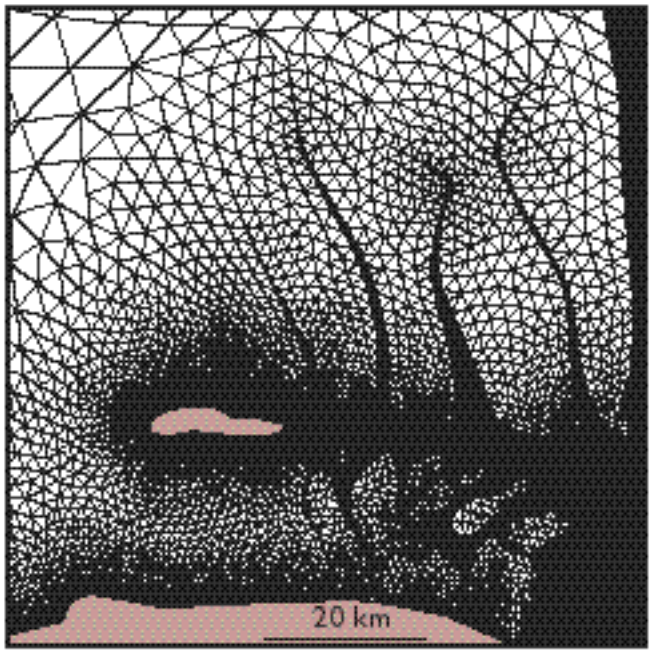

Figure 3.

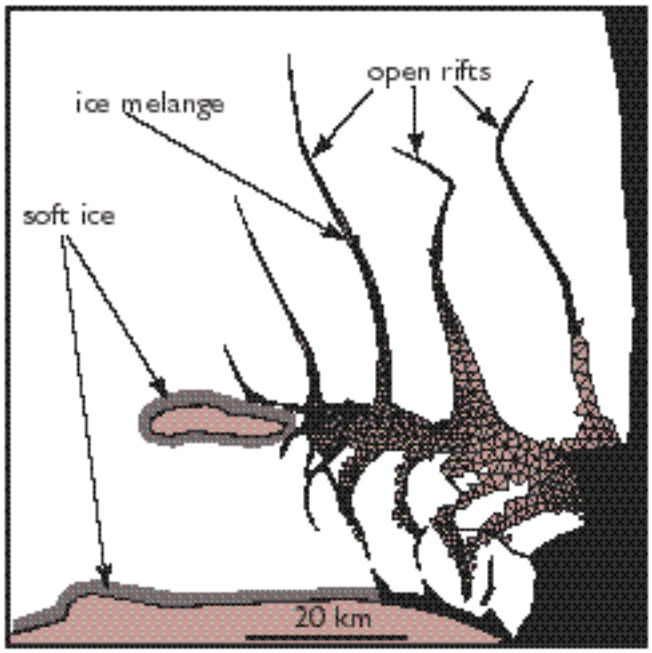

Figure 4.

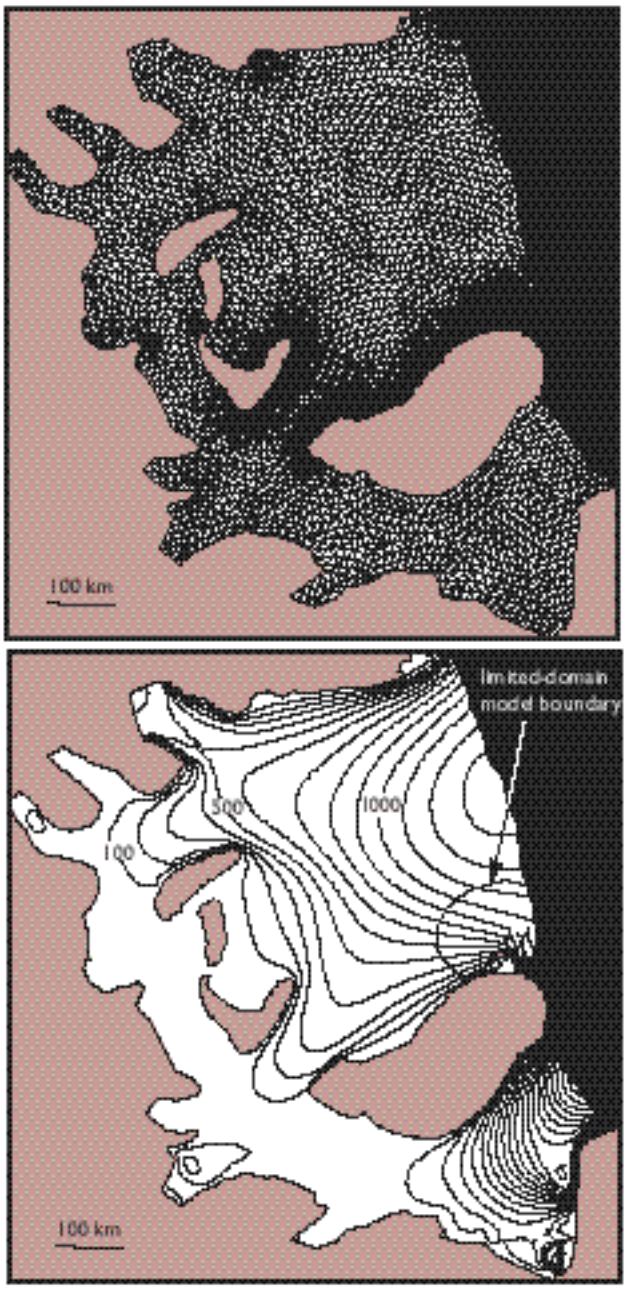

Figure 5.

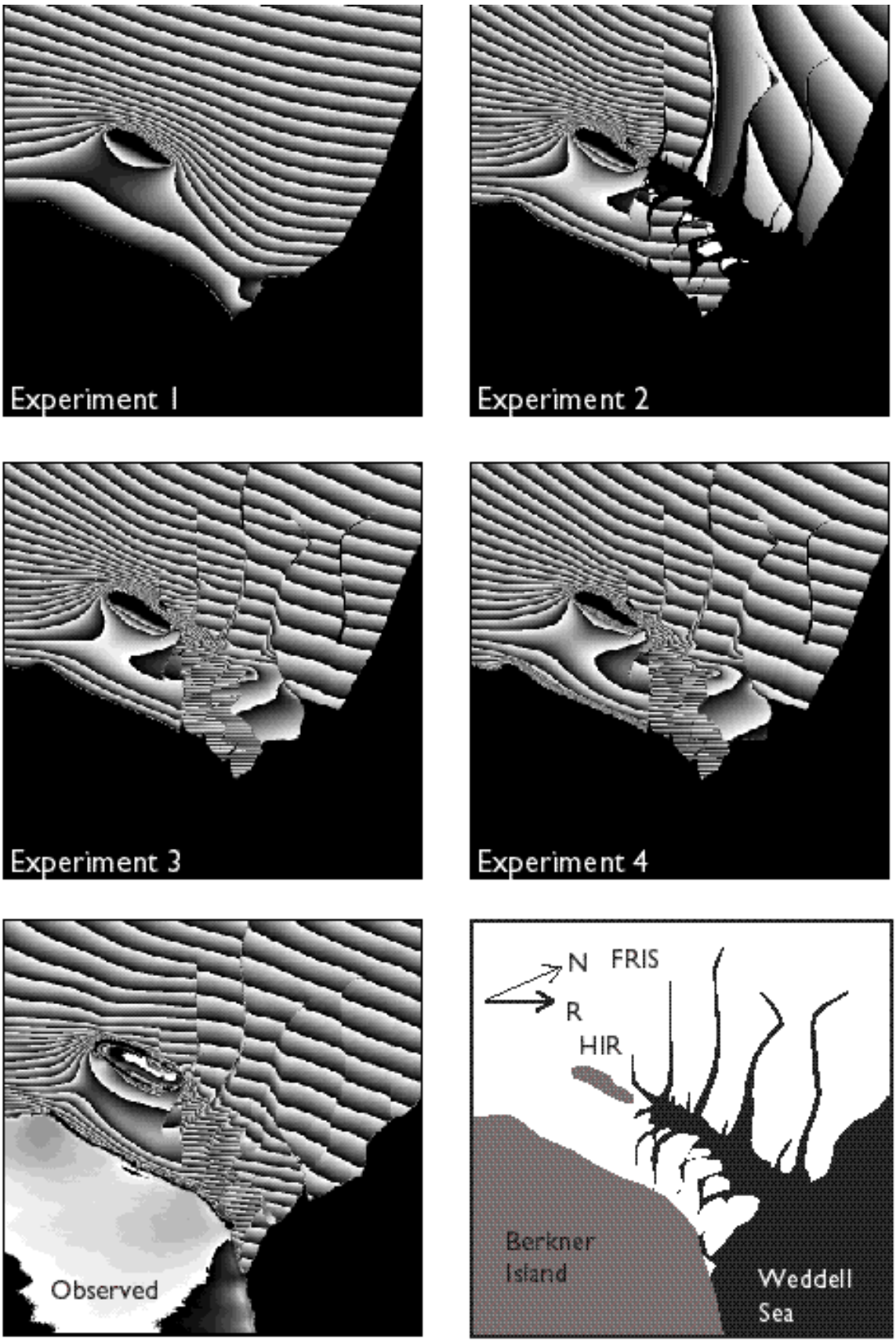
Experiment 1
Experiment 2
Experiment 3
Experiment 4
Observed
N
FRIS
R
HIR
Berkner
Island
Weddell
Sea

Figure 6.

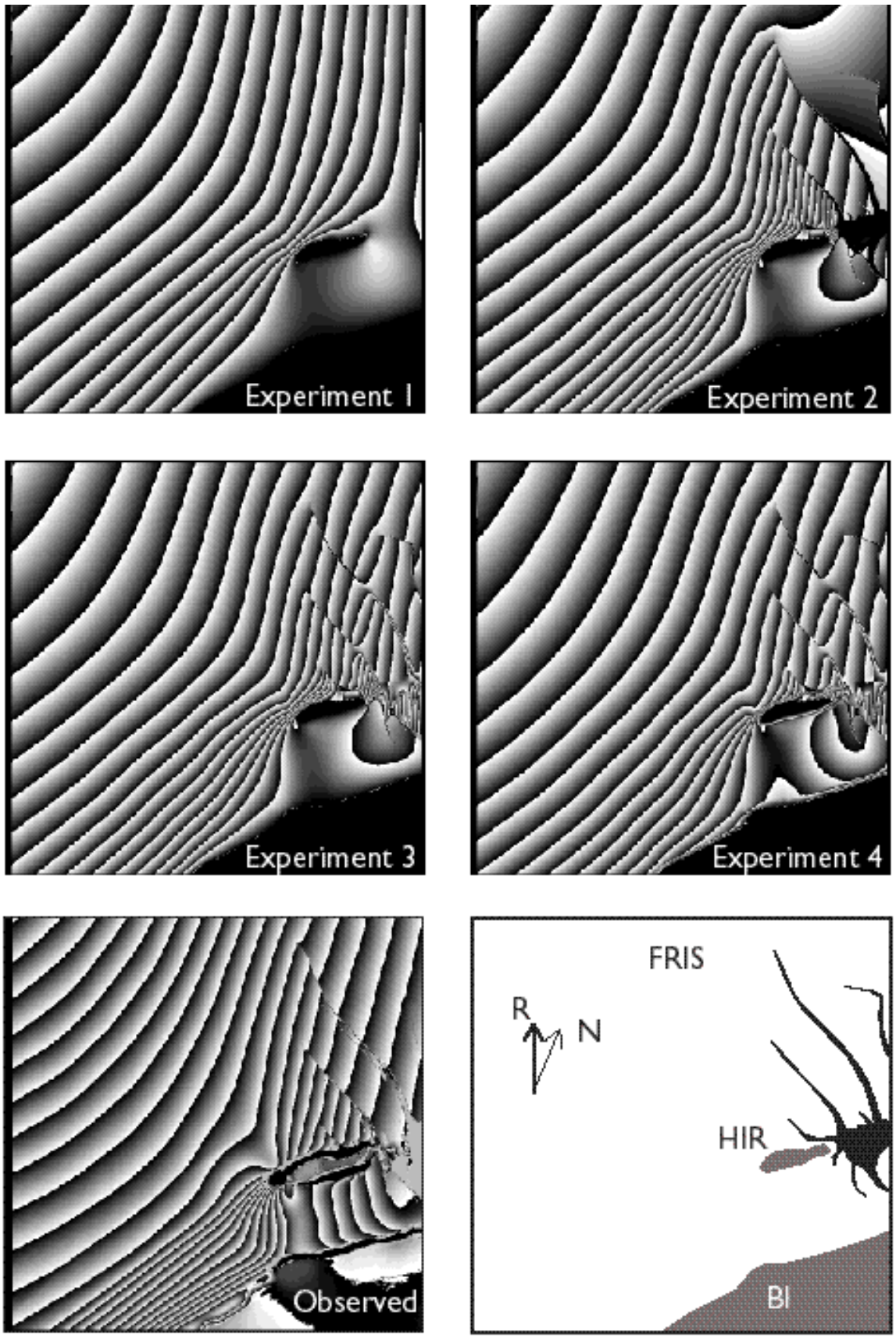
Experiment 1
Experiment 2
Experiment 3
Experiment 4
Observed
FRIS
R
N
HIR
BI

Figure 7.

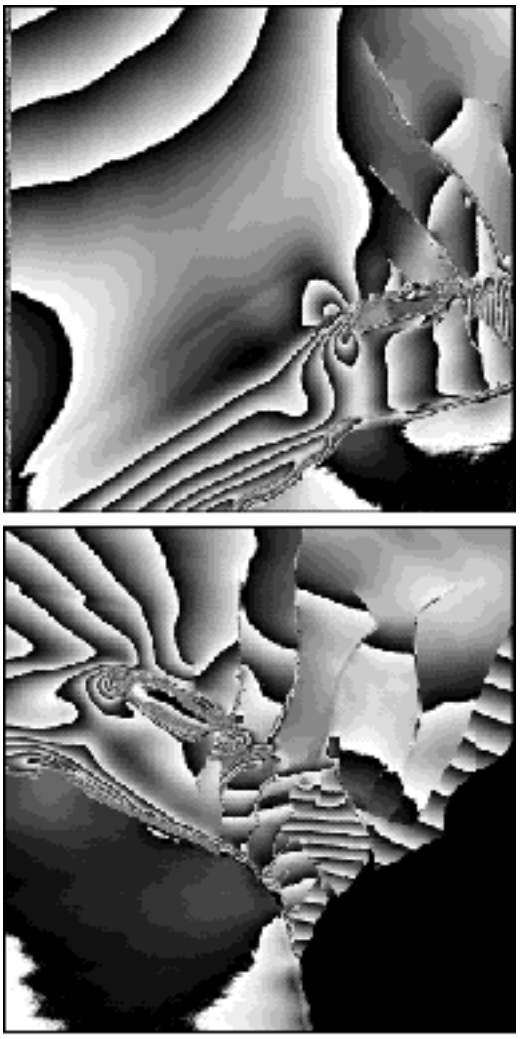

Figure 8.

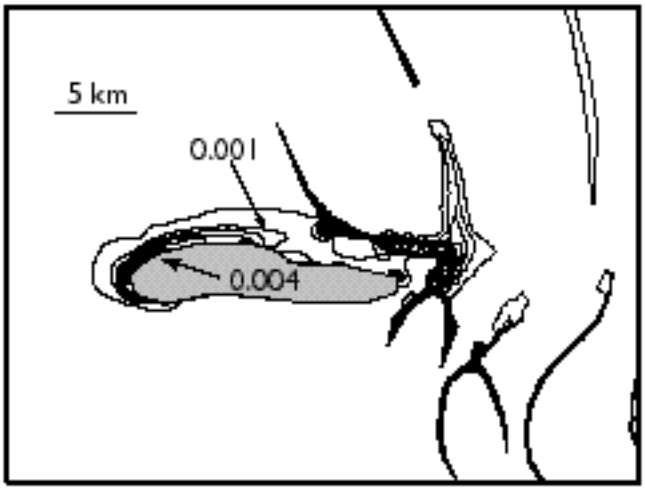

Figure 9.